



ORIGINAL RESEARCH ARTICLE

# Photocatalytic Application of Ag-Decorated CuS/BaTiO<sub>3</sub> Composite Photocatalysts for Degrading RhB

YANPING WANG,<sup>1</sup> RUIZHAN LI,<sup>1</sup> XIAOFENG SUN,<sup>2</sup> TAO XIAN,<sup>2</sup> ZAO YI,<sup>3</sup>  
and HUA YANG <sup>1,4</sup>

1.—State Key Laboratory of Advanced Processing and Recycling of Non-Ferrous Metals, Lanzhou University of Technology, Lanzhou 730050, China. 2.—College of Physics and Electronic Information Engineering, Qinghai Normal University, Xining 810008, China. 3.—Joint Laboratory for Extreme Conditions Matter Properties, Southwest University of Science and Technology, Mianyang 621010, China. 4.—e-mail: hyang@lut.cn

Herein, binary CuS/BTO and ternary CuS/Ag/BTO composite photocatalysts have been fabricated by anchoring CuS and Ag nanoparticles onto BaTiO<sub>3</sub> (BTO) polyhedra. The as-prepared composite photocatalysts were characterized by means of the techniques of transmission/scanning electron microscopy, x-ray powder diffraction, ultraviolet–visible diffuse reflectance spectroscopy, x-ray photoelectron spectroscopy and photoluminescence spectroscopy. Transient photocurrent and electrochemical impedance spectroscopy measurements suggest that the ternary 5%CuS/(1%Ag/BTO) composite possesses the highest separation efficiency of electron/hole pairs. The photodegradation experiments were conducted by using simulated sunlight as the light source to decompose Rhodamine B in water solution. The 5%CuS/(1%Ag/BTO) and 5%CuS/BTO composites are demonstrated to have the highest and second highest photodegradation activity, respectively. As compared with that of bare BaTiO<sub>3</sub> and CuS, the photoactivity of 5%CuS/(1%Ag/BTO) is increased to 3.3 and 2.0 times, respectively. The electron/hole separation mechanism and the role of localized surface plasmon resonance of Ag nanoparticles in the dye photodegradation were systematically investigated.

**Key words:** BaTiO<sub>3</sub> polyhedra, CuS/BaTiO<sub>3</sub> heterojunctions, CuS/Ag/BaTiO<sub>3</sub> composites, photodegradation performances

## INTRODUCTION

Nowadays, the arbitrarily discharged effluent from chemical industries is causing serious pollution to water resources. To remove toxic and carcinogenic substances (e.g., organic dyes) from industrial effluent has become a big research topic to protect our living environment. In recent years, photocatalysis technology based on semiconductor materials has gained much attention in the remediation of water resources.<sup>1–4</sup> The unique advantage of this effluent treatment technology is that it is capable of decomposing toxic organic dyes under

solar irradiation. Solar irradiation excites semiconductor photocatalysts to generate electrons ( $e^-$ ) and holes ( $h^+$ ) in their conduction band (CB) and valence band (VB), respectively. Benefiting from their reduction (electrons) and oxidation (holes) capacities, the photoexcited electrons/holes directly or indirectly act upon the pollutants to cause their decomposition. Nevertheless, only a few photoexcited electrons/holes are available for the photodegradation reactions because of their high geminate recombination. In order to improve the photocatalytic activity of semiconductors, it is indispensable in increasing the probability of photoexcited carriers for participating in the photoreactions. Therefore, various avenues have been adopted to prolong the carrier lifetime by spatially separating the  $e^-/h^+$  pairs.<sup>5–8</sup>

(Received September 30, 2020; accepted January 27, 2021; published online February 17, 2021)

Coupling two semiconductors into heterojunctions is one of the important strategies to inhibit the recombination of photoproduced electrons and holes.<sup>9–11</sup> As expected, an internal electric field is created at the interface of the semiconductor–semiconductor heterojunctions. Under the action of an internal electric field, the photogenerated electrons/holes will be driven from one semiconductor to another. This is the dominant mechanism decreasing the geminate  $e^-/h^+$  recombination in the heterojunction composite photocatalysts. Another intriguing method to enhance the  $e^-/h^+$  spatial separation is to decorate electron traps onto the semiconductor photocatalysts.<sup>12–16</sup> The most important electron traps include graphene, carbon nanofibers/nanotubes/quantum dots and noble metal nanoparticles. These nanosized carbon and noble metal materials are particularly interesting and have received much attention due to their fascinating physical properties and potential technological applications in many fields.<sup>17–20</sup> Moreover, the excellent electron-trapping ability of these nanosized materials makes it easier for them to trap the photoproduced electrons, thus reducing the  $e^-/h^+$  recombination probability. These nanomaterials can also act as interesting co-catalysts. For example, nanosized noble metals commonly exhibit strong visible-light absorption due to their localized surface plasmon resonance (LSPR) effect, which implies that they can efficiently utilize visible light to drive the photodegradation reactions.<sup>21,22</sup> Development of ternary composite photocatalysts by simultaneously constructing heterojunctions and decorating nanosized noble metals is expected to be a promising strategy to achieve superior photodegradation performances.

Ti-oxide semiconductors have been received as the most important candidate photocatalysts in the application of industrial wastewater purification.<sup>7,23–25</sup> The perovskite-structured barium titanate (BaTiO<sub>3</sub>, BTO) is a typical example of Ti-oxide semiconductors, famously known for its piezoelectricity and ferroelectricity.<sup>26</sup> In addition to the intriguing physical properties, BaTiO<sub>3</sub> is particularly interesting due to its photodegradation capability for decomposing organic dyes.<sup>27,28</sup> Moreover, BaTiO<sub>3</sub> also stands out due to its high chemical/photo-corrosion resistance, good stability, abundant natural resources, low cost, environmental friendliness, and easy fabrication. These advantages suggest that BaTiO<sub>3</sub> is an excellent candidate for potential applications in environmental purification. However, the large band gap energy of BaTiO<sub>3</sub> ( $\sim 3.2$  eV) limits its photoactivity to the ultraviolet (UV) region, which occupies only a small fraction of solar energy.<sup>29,30</sup> In contrast, another promising photocatalyst–covellite (CuS) has a relatively narrower band gap ( $\sim 2.0$  eV), making it photoactive in a wide solar spectrum.<sup>31,32</sup> For both pristine BaTiO<sub>3</sub>

and CuS, their photocatalytic efficiencies are not satisfying owing to the easy  $e^-/h^+$  recombination. To overcome this shortcoming, many avenues have been adopted to improve the photodegradation performances of BaTiO<sub>3</sub> and CuS, e.g., construction of heterojunctions and decoration with noble metal nanoparticles.<sup>33–37</sup> It is noted that the CB/VB positions between BaTiO<sub>3</sub> and CuS are staggered with each other, indicating that they can be coupled to form promising CuS/BTO heterojunctions.

In the present work, we have constructed CuS/BTO heterojunction photocatalysts by incorporating smaller-sized CuS nanoparticles onto larger-sized BaTiO<sub>3</sub> polyhedral particles. The effect of the CuS content on the photodegradation performance of the CuS/BTO composites was investigated and the optimal composite photocatalyst was determined. Then, the optimal CuS/BTO composite was decorated with Ag nanoparticles to obtain ternary CuS/Ag/BTO composite photocatalysts. Rhodamine B (RhB), known as a typical organic dye present in industry-produced wastewater, was used as the target pollutant to evaluate the photodegradation capabilities of the as-prepared composite photocatalysts under simulated-sunlight irradiation.

## EXPERIMENTAL

### Synthesis of BaTiO<sub>3</sub> Polyhedral Particles and CuS Nanoparticles

Analytical-grade chemical reagents, derived from chemical reagent corporations in China, were used in the present experiments. A hydrothermal reaction process was employed to synthesize BaTiO<sub>3</sub> polyhedral particles. First, three types of solutions, separately denoted as A, B and C, were prepared. Solution A was obtained by dissolving 1.0454 g (4 mmol) of Ba(NO<sub>3</sub>)<sub>2</sub> in 20 mL deionized water, solution B was prepared by dissolving 2.4688 g (44 mmol) of KOH in 20 mL deionized water, and solution C was derived by adding 10 mL of oleic acid and 1.0892 g (3.2 mmol) of *tetra-n*-butyl titanate (C<sub>16</sub>H<sub>36</sub>O<sub>4</sub>Ti) to 20 mL *n*-butanol. Every step mentioned above was accompanied by 30 min of magnetic stirring to ensure that a uniform solution was obtained. Next, solutions C and B were successively dropped into solution A with 30 min of magnetic stirring. Then, the resultant mixture solution was sealed in a 100-mL Teflon-lined autoclave and subjected to the hydrothermal reaction (200°C, 24 h). Finally, the precipitate produced in the autoclave was collected as BaTiO<sub>3</sub> particles by centrifugation. To remove impurity phases and ions, the product was rinsed with 10% (V/V) dilute nitric acid (one time), deionized water (three times) and anhydrous alcohol (three times), followed by drying in an electrothermal constant-temperature dry oven (60°C, 12 h).

CuS nanoparticles were obtained via a coprecipitation synthesis method. Stoichiometric amounts of  $\text{Cu}(\text{NO}_3)_2 \cdot 3\text{H}_2\text{O}$  (0.4832 g) and  $\text{Na}_2\text{S} \cdot 9\text{H}_2\text{O}$  (0.4802 g) were dissolved in 30 mL and 20 mL ethylene glycol with magnetic stirring for 30 min, respectively. The obtained  $\text{Na}_2\text{S}$  solution was slowly added into the  $\text{Cu}(\text{NO}_3)_2$  solution, which was then magnetically stirred for 30 min at room temperature (20°C). The precipitated product was collected as CuS nanoparticles by centrifugation. A rinsing process using deionized water (three times) and anhydrous ethanol (three times) was required to remove impurity ions from the product.

### Construction of CuS/BTO Composites

To prepare the 5%CuS/BTO composite (CuS occupies a mass fraction of 5% in the composite), 0.3 g of as-prepared  $\text{BaTiO}_3$  particles was loaded in 30 mL ethylene glycol (ultrasonic dispersion for 30 min), which was then dissolved with 0.0399 g of  $\text{Cu}(\text{NO}_3)_2 \cdot 3\text{H}_2\text{O}$  (magnetic stirring for 30 min). The  $\text{Na}_2\text{S}$  solution, which was obtained by dissolving 0.0397 g of  $\text{Na}_2\text{S} \cdot 9\text{H}_2\text{O}$  in 20 mL ethylene glycol with 30 min magnetic stirring, was slowly dropped into the above suspension. The resultant mixture was magnetically stirred at room temperature for 30 min, during which CuS nanoparticles were crystallized and assembled on the surface of  $\text{BaTiO}_3$  particles. After washing and drying, the final 5%CuS/BTO composite was obtained. Based on the same route, the 3%CuS/BTO and 8%CuS/BTO composites were also prepared by loading different

amounts of  $\text{BaTiO}_3$  particles in the precursor solution.

### Construction of CuS/Ag/BTO Composites

A typical ternary 5%CuS/(1%Ag/BTO) composite photocatalyst was prepared as follows. First, the 1%Ag/BTO composite was prepared by decorating Ag nanoparticles on the surface of  $\text{BaTiO}_3$  particles via a photoreduction method. Next, 0.3 g of  $\text{BaTiO}_3$  particles and 0.025 g of ammonium oxalate (AO) were loaded in 80 mL deionized water with 30 min of ultrasonic dispersion and then 60 min of magnetic stirring. Then, 0.14 mL of  $0.2 \text{ mol L}^{-1}$   $\text{AgNO}_3$  aqueous solution was added to the above suspension. A 15-W low-pressure mercury lamp (emitting UV light) was used to illuminate the resultant mixture for 30 min under magnetic stirring, during which Ag nanoparticles were formed on the  $\text{BaTiO}_3$  particle surface. The product was collected as the 1%Ag/BTO composite after rinsing and drying. Then, the derived 1%Ag/BTO composite was decorated with CuS nanoparticles to form the ternary 5%CuS/(1%Ag/BTO) composite. The decoration procedure was same to that for preparing 5%CuS/BTO, as elaborated above. The preparation process for the CuS/BTO and CuS/Ag/BTO composites is schematically depicted in Fig. 1.

### Characterization of Samples

Various material characterization technologies including x-ray powder diffraction (XRD), transmission/scanning electron microscopy (TEM/SEM),

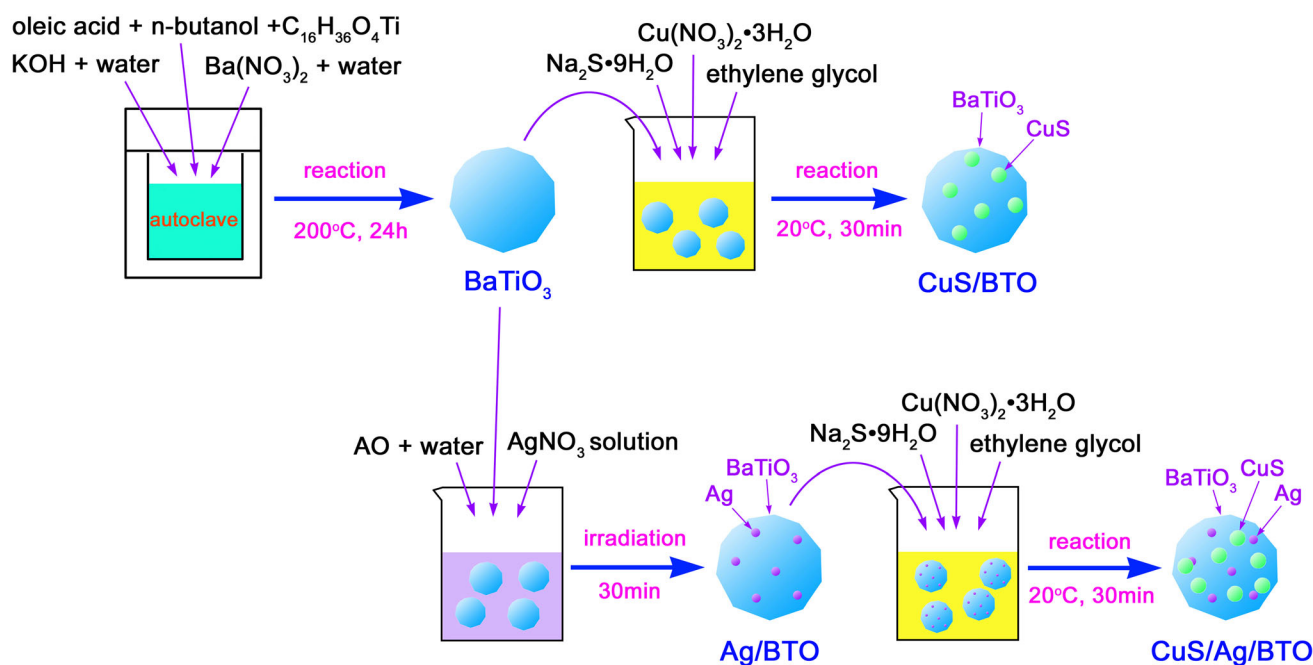


Fig. 1. Schematic preparation process for CuS/BTO and CuS/Ag/BTO composite photocatalysts.

energy-dispersive x-ray spectroscopy (EDS), ultra-violet-visible (UV-Vis) diffuse reflectance spectroscopy (DRS), x-ray photoelectron spectroscopy (XPS) and photoluminescence (PL) spectroscopy were employed to elucidate the structures, morphologies, microstructures, optical absorption properties, chemical composition, elemental valence states and PL properties of the as-prepared photocatalysts. The XRD analysis was carried out on a D8 Advance x-ray diffractometer ( $\lambda_{\text{Cu-}k\alpha} = 0.15406 \text{ nm}$ ). A field-emission transmission electron microscope (JEM-1200EX) and a scanning electron microscope (JSM-6701F) were employed for the TEM/SEM investigations. UV-Vis DRS spectra were recorded on a TU-1901 double beam spectrophotometer. XPS spectra were derived from a multi-functional x-ray photoelectron spectrometer (PHI-5702). A RF-6000 fluorescence spectrophotometer was used to record the PL spectra (excitation wavelength: 290 nm).

A three-electrode structure including a platinum foil electrode as the counter electrode and a standard calomel electrode (SCE) as the reference electrode was employed for the photocurrent response and electrochemical impedance spectroscopy (EIS) measurements on a CST 350 electrochemical workstation.  $0.1 \text{ mol L}^{-1} \text{ Na}_2\text{SO}_4$  water solution was used as the electrolyte. A 200-W xenon lamp was used as the sunlight simulator. The procedures for the working electrode preparation and photoelectrochemical measurements were discussed in detail in our previously published papers.<sup>38</sup>

### Photodegradation Experiments

The target contaminant selected was  $5 \text{ mg L}^{-1}$  RhB water solution to study the decomposition capacities of the as-prepared photocatalysts. The photocatalyst concentration was set as  $C_{\text{photocatalyst}} = 0.3 \text{ g L}^{-1}$  by loading 0.03 g of the photocatalyst into 100 mL RhB solution. The mixture solution was put into a 200-mL photoreactor and then magnetically stirred in the dark for 30 min to examine the RhB adsorption onto the photocatalyst. After that, the photodegradation experiment was initiated by irradiating the reaction solution with simulated sunlight emitted from a 200-W xenon lamp. The distance between the front of the lamp and the reaction solution is 15 cm. The photoreactor was cooled by circulating water so as to maintain the reaction solution at room temperature ( $20^\circ\text{C}$ ). As time progressed, the change of the RhB concentration was examined by withdrawing a small amount of the reaction solution (2.5 mL) and measuring its absorbance. After removing the photocatalyst by centrifugation, the absorbance of the reaction solution was measured by using a UV-Vis spectrophotometer (measuring wavelength: 554 nm). The degradation ratio ( $\eta$ ) of RhB can be derived according to the relationship  $\eta = (C_0 - C_t)/$

$C_0 \times 100\%$ , where  $C_0$  and  $C_t$  are the initial and residual RhB concentrations, respectively.

## RESULTS AND DISCUSSION

Figure 2a displays the XRD patterns recorded from the as-prepared CuS, BaTiO<sub>3</sub>, 5%CuS/BTO and 5%CuS/(1%Ag/BTO) photocatalysts. The XRD pattern of BaTiO<sub>3</sub> presents the characteristic diffraction peaks at  $22.2^\circ$ ,  $31.6^\circ$ ,  $38.9^\circ$ ,  $45.2^\circ$ ,  $50.9^\circ$  and  $56.2^\circ$ , which match well with the (100), (110), (111), (200), (210) and (211) facets of the BaTiO<sub>3</sub> cubic phase (PDF#79-2263), respectively. The XRD pattern of CuS shows the diffraction peaks agreeing perfectly with those of the hexagonal phase of CuS (PDF#06-0464). The XRD data suggest that bare BaTiO<sub>3</sub> and CuS are crystallized into a pure cubic structure and a hexagonal structure, respectively. The XRD patterns of 5%CuS/BTO and 5%CuS/(1%Ag/BTO) are very similar to that of bare BaTiO<sub>3</sub>, where all the diffraction peaks can be indexed into the cubic BaTiO<sub>3</sub>. The diffraction peaks of CuS and Ag are not clearly detectable on the XRD patterns, which is due to their low contents in the composites. However, the apparent colors and optical absorption properties of the samples confirm the decoration of CuS and Ag onto BaTiO<sub>3</sub>. As seen from Fig. 2b, bare BaTiO<sub>3</sub> and CuS appear in cream white and black, respectively. In contrast, the 5%CuS/BTO and 5%CuS/(1%Ag/BTO) composites present as gray, which is obviously deeper than that of bare BaTiO<sub>3</sub>. It is noted that the physical properties of materials depend highly on their light absorption characteristics, which are necessary to characterize.<sup>39,40</sup> Figure 2c illustrates the UV-Vis DRS spectra of the samples, from which one can see that bare BaTiO<sub>3</sub> has a weak absorption in the visible-light region, whereas a strong visible-light absorption is observed for bare CuS. The 5%CuS/BTO and 5%CuS/(1%Ag/BTO) composites display a visible-light absorption that is obviously stronger than bare BaTiO<sub>3</sub>. The differential curves of the UV-Vis DRS spectra can be employed to estimate the band gap ( $E_g$ ) of BaTiO<sub>3</sub> in the samples,<sup>41</sup> as shown in Fig. 2d. According to the peak on the differential spectra (i.e. absorption edge), the band gap of BaTiO<sub>3</sub> is obtained as 3.26 eV for bare BaTiO<sub>3</sub> and 3.34 eV for 5%CuS/BTO and 5%CuS/(1%Ag/BTO). The slightly increased band gap of BaTiO<sub>3</sub> in the composites may be ascribed to the interaction of BaTiO<sub>3</sub> with CuS and Ag. The Tauc plot of  $(\alpha h\nu)^2$  versus  $h\nu$ , which is transformed from the DRS spectrum of CuS, is used for determining the band gap of CuS.<sup>42</sup> As seen from the inset in Fig. 2d, the band gap of CuS is obtained as 2.02 eV by extrapolating the linear region of the Tauc plot to the  $h\nu$ -axis.

SEM images were recorded from BaTiO<sub>3</sub>, CuS, 5%CuS/BTO and 5%CuS/(1%Ag/BTO) to reveal their morphologies and sizes, as illustrated in Fig. 3. It is observed from Fig. 3a that BaTiO<sub>3</sub> is

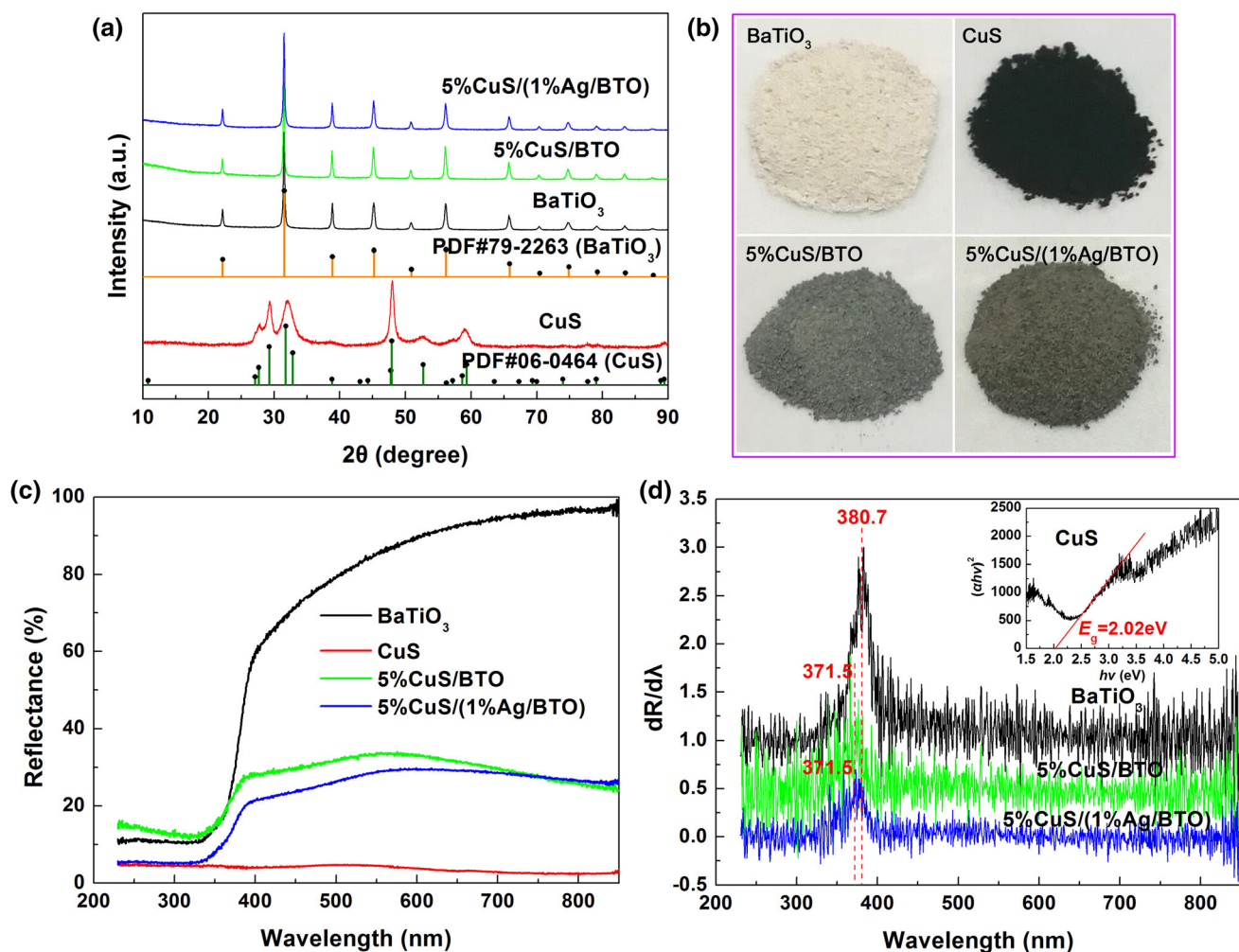


Fig. 2. XRD patterns (a), apparent colors (b), UV-Vis DRS spectra (c) and differential curves of the DRS spectra (d) of CuS, BaTiO<sub>3</sub>, 5%CuS/BTO and 5%CuS/(1%Ag/BTO). The inset in (d) shows the Tauc plot of  $(\alpha h\nu)^2$  versus  $h\nu$  for CuS.

crystallized as polyhedral particles with diameter ranging from 50 nm to 110 nm. The SEM image presented in Fig. 3b reveals the synthesis of spherical CuS nanoparticles with size of 10–25 nm. The SEM image of 5%CuS/BTO (Fig. 3c) demonstrates the decoration of smaller-sized CuS nanoparticles onto larger-sized BaTiO<sub>3</sub> polyhedra. As seen from Fig. 3d, the 5%CuS/(1%Ag/BTO) photocatalyst is composed of BaTiO<sub>3</sub> polyhedra decorated with CuS and Ag nanoparticles.

The microstructure of the 5%CuS/(1%Ag/BTO) composite was further investigated by means of TEM related techniques. Figure 4a illustrates the TEM image of the 5%CuS/(1%Ag/BTO) composite, revealing the good coupling of BaTiO<sub>3</sub> polyhedra with CuS and Ag nanoparticles. The derived selected area electron diffraction (SAED) pattern (Fig. 4b) shows clear diffraction spots or rings, suggesting that the composite has a good crystallization degree. By comparing the diffraction spots/rings with the standard diffraction data of BaTiO<sub>3</sub>, CuS and Ag, it is found that they can be perfectly indexed in terms of BaTiO<sub>3</sub>, CuS and Ag. The

measured high-resolution TEM (HRTEM) images, as depicted in Fig. 4c and d, further confirm the coupling of BaTiO<sub>3</sub> polyhedra with CuS/Ag nanoparticles and their perfect crystalline features. The BaTiO<sub>3</sub> polyhedral particles show the characteristic (110) lattice fringes with the  $d$ -spacing of 0.283 nm. The CuS nanoparticles are recognized by their characteristic lattice fringes with  $2d_{008} = 0.409$  nm or  $d_{103} = 0.281$  nm. The nanoparticle with lattice fringes of 0.237 nm, matching perfectly with the  $d_{111}$  spacing of Ag, is confirmed to be the Ag nanoparticle.

Figure 5a shows the TEM-EDS spectrum of 5%CuS/(1%Ag/BTO), suggesting the existence of Ba/Ti/Cu/S/O/Ag in the composite. The extremely high intensity of the Cu peaks may be induced by additional Cu from the microgrid holder.<sup>43</sup> EDS elemental mapping was adopted to investigate the elemental distribution in the composite. Figure 5b shows the dark-field scanning TEM (DF-STEM) image of the 5%CuS/(1%Ag/BTO) composite. The area outlined by an orange rectangle in Fig. 5b is investigated by EDS elemental mapping. As seen

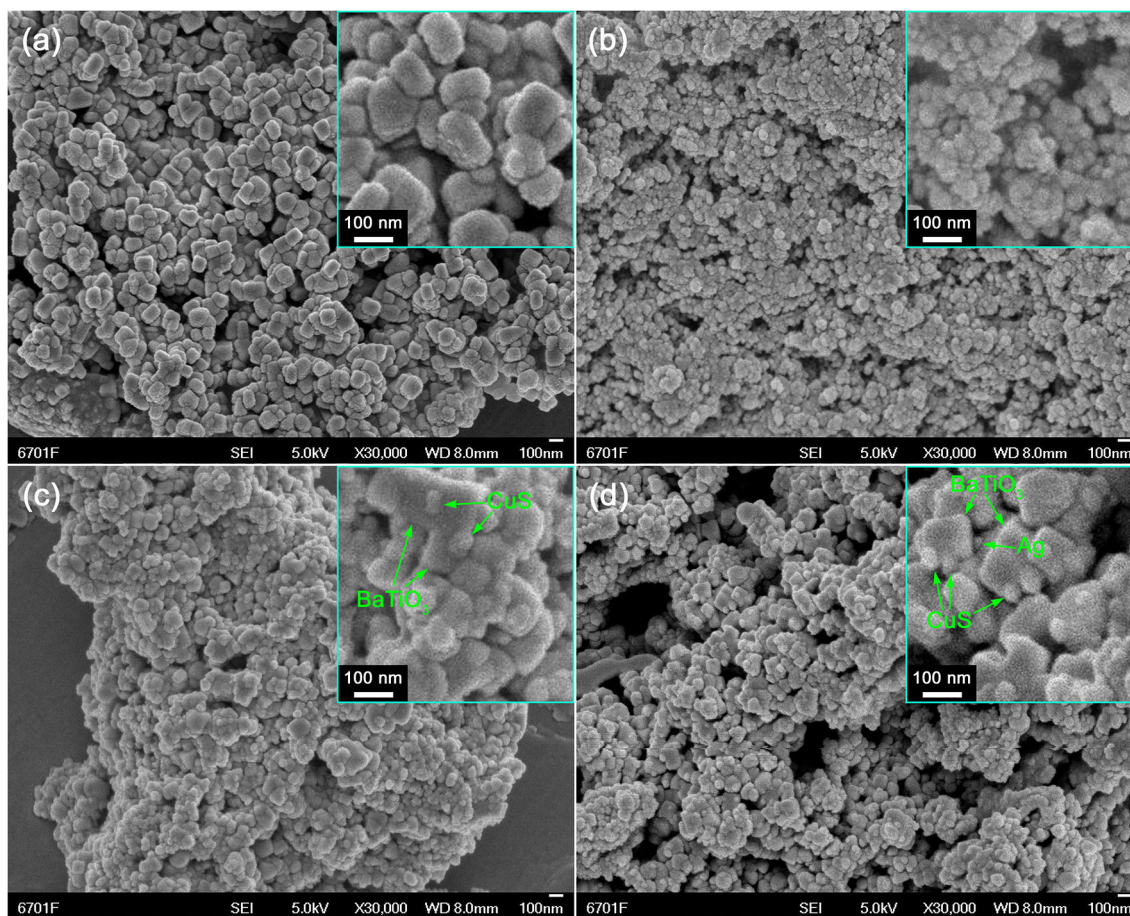


Fig. 3. SEM images of (a) BaTiO<sub>3</sub>, (b) CuS, (c) 5%CuS/BTO and (d) 5%CuS/(1%Ag/BTO).

from the derived mapping images in Fig. 5c–h, in addition to Ba/Ti/O uniformly existing in the composite, Cu/S/Ag are also distributed throughout the composite. The elemental mapping results are indicative of the coupling of BaTiO<sub>3</sub> polyhedra with CuS and Ag nanoparticles.

XPS is a useful technology that can be used for the diagnosis of element valences.<sup>44</sup> The XPS spectra of 5%CuS/(1%Ag/BTO) including Ba-3*d*, Ti-2*p*, O-1*s*, Cu-2*p*, S-2*p* and Ag-3*d* core-level XPS spectra are collected in order to reveal the valence states of the elements. The characteristic Ba-3*d* XPS spectrum presented in Fig. 6a (Ba-3*d*<sub>5/2</sub> → 779.2 eV, Ba-3*d*<sub>3/2</sub> → 794.6 eV) and Ti-2*p* XPS spectrum given in Fig. 6b (Ti-2*p*<sub>3/2</sub> → 458.7 eV, Ba-2*p*<sub>1/2</sub> → 464.4 eV) indicate the existence of Ba<sup>2+</sup> and Ti<sup>4+</sup> species in the composite.<sup>33,45</sup> Two binding-energy peaks (530.0 eV and 531.7 eV) are observed on the O-1*s* XPS spectrum (Fig. 6c), of which the peak at 530.0 eV originates from the crystal lattice oxygen of BaTiO<sub>3</sub>,<sup>33,45</sup> and the peak at 531.7 eV has contributions from the chemisorbed oxygen species.<sup>46</sup> The Cu<sup>2+</sup> species is confirmed by the Cu-2*p* XPS spectrum (Fig. 6d) with characteristic Cu-2*p*<sub>3/2</sub> binding energy at 932.1 eV and Cu-2*p*<sub>1/2</sub> binding energy at 952.1 eV.<sup>38</sup> On the S-2*p* XPS spectrum (Fig. 6e), the peaks at 160.7 eV and

162.1 eV are characterized as the S<sup>2-</sup>-2*p*<sub>3/2</sub> and S<sup>2-</sup>-2*p*<sub>1/2</sub> binding energies, respectively. The characteristic peaks detected on the Ag-3*d* XPS spectrum (Fig. 6f) suggest that the Ag species appears in the metallic state (Ag-3*d*<sub>5/2</sub> → 367.6 eV, Ba-3*d*<sub>3/2</sub> → 373.6 eV).<sup>33</sup>

The photoexcited carrier separation behavior is an important factor that significantly influences the photodegradation performance of photocatalysts, which can be characterized by PL spectroscopy.<sup>47,48</sup> As seen from Fig. 7, the PL spectra collected from all the samples show a broad PL emission peak at 380 nm, but their intensities are different. The PL emission peak is related to the recombination behavior of photoexcited electrons and holes. It is obvious that the coupling of BaTiO<sub>3</sub> with CuS and Ag results in the decrease in the PL emission peak when compared with that of bare BaTiO<sub>3</sub>; noticeably, the PL emission peak from 5%CuS/(1%Ag/BTO) becomes the weakest. This suggests that the highest photodegradation activity will be achieved for the 5%CuS/(1%Ag/BTO) composite due to its highest *e*<sup>-</sup>/*h*<sup>+</sup> separation efficiency.

Photoelectrochemical measurement is an alternative method that can be used to elaborate the separation behavior of photoexcited charges in photocatalysts. Transient photocurrent response

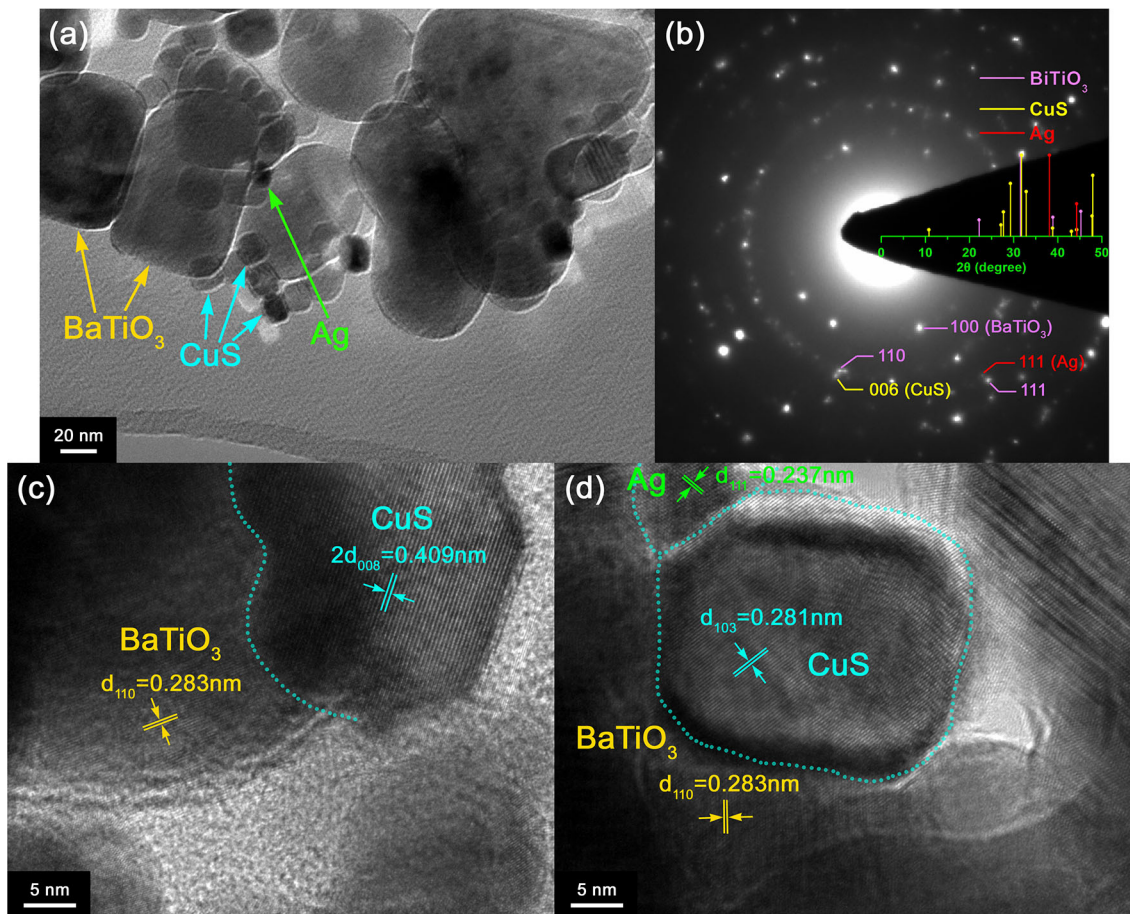


Fig. 4. TEM image (a), SAED pattern (b) and HRTEM images (c,d) of 5%CuS/(1%Ag)/BTO.

curves recorded from BaTiO<sub>3</sub>, 3%CuS/BTO, 5%CuS/BTO, 8%CuS/BTO and 5%CuS/(1%Ag)/BTO are presented in Fig. 8a. It is seen that the intermittent irradiation of the photocatalysts results in the periodic appearance of photocurrent in them. The observed photocurrent for the samples appears in the following order: BaTiO<sub>3</sub> < 3%CuS/BTO < 8%CuS/BTO < 5%CuS/BTO < 5%CuS/(1%Ag)/BTO. This implies that the  $e^-/h^+$  separation efficiency is enhanced for the composite photocatalysts compared to bare BaTiO<sub>3</sub>; noticeably, the 5%CuS/(1%Ag)/BTO composite has the highest  $e^-/h^+$  separation efficiency. The EIS Nyquist spectra are also recorded and displayed in Fig. 8b. The diameter of the semicircle observed in the region of high frequencies is induced by the charge-transfer resistance and can reflect the photoexcited charge separation efficiency in the photocatalysts.<sup>49</sup> The EIS observed result is basically in agreement with that obtained by PL spectroscopy and transient photocurrent spectroscopy.

Figure 9a presents the adsorption and photodegradation performances of all the as-prepared samples for RhB driven by simulated sunlight. It is seen that with 30 min of adsorption in the dark,

3.5% and 46.3% of RhB is adsorbed onto bare BaTiO<sub>3</sub> and CuS photocatalysts, respectively. The extremely large RhB adsorption for CuS may be because the -OH groups attached to CuS have a strong electrostatic attraction to cationic RhB molecules.<sup>50</sup> The blank experiment in the absence of photocatalysts shows that RhB appears to be fairly stable under simulated sunlight irradiation. The CuS/BTO and 5%CuS/(1%Ag)/BTO composite photocatalysts exhibit a dye adsorption higher than that for bare BaTiO<sub>3</sub> due to the introduction of CuS. The photodegradation behaviors of the samples are elaborated by the decrease in the RhB concentration with increasing the irradiation time. The degradation ratio  $\eta$  of RhB by irradiating the photocatalytic systems for 120 min (Table I) is in the order: BaTiO<sub>3</sub> < CuS < 3%CuS/BTO < 8%CuS/BTO < 5%CuS/BTO < 5%CuS/(1%Ag)/BTO. The largest and second largest photodegradation activities are observed for 5%CuS/(1%Ag)/BTO and 5%CuS/BTO, respectively. It is obvious that the integration of BaTiO<sub>3</sub> polyhedra with CuS and Ag nanoparticles can generate excellent composite photocatalysts with enhanced photoactivities. Figure 9b shows the plots of  $\ln(C_0/C_t)$  against irradiation time  $t$ , which are linearly

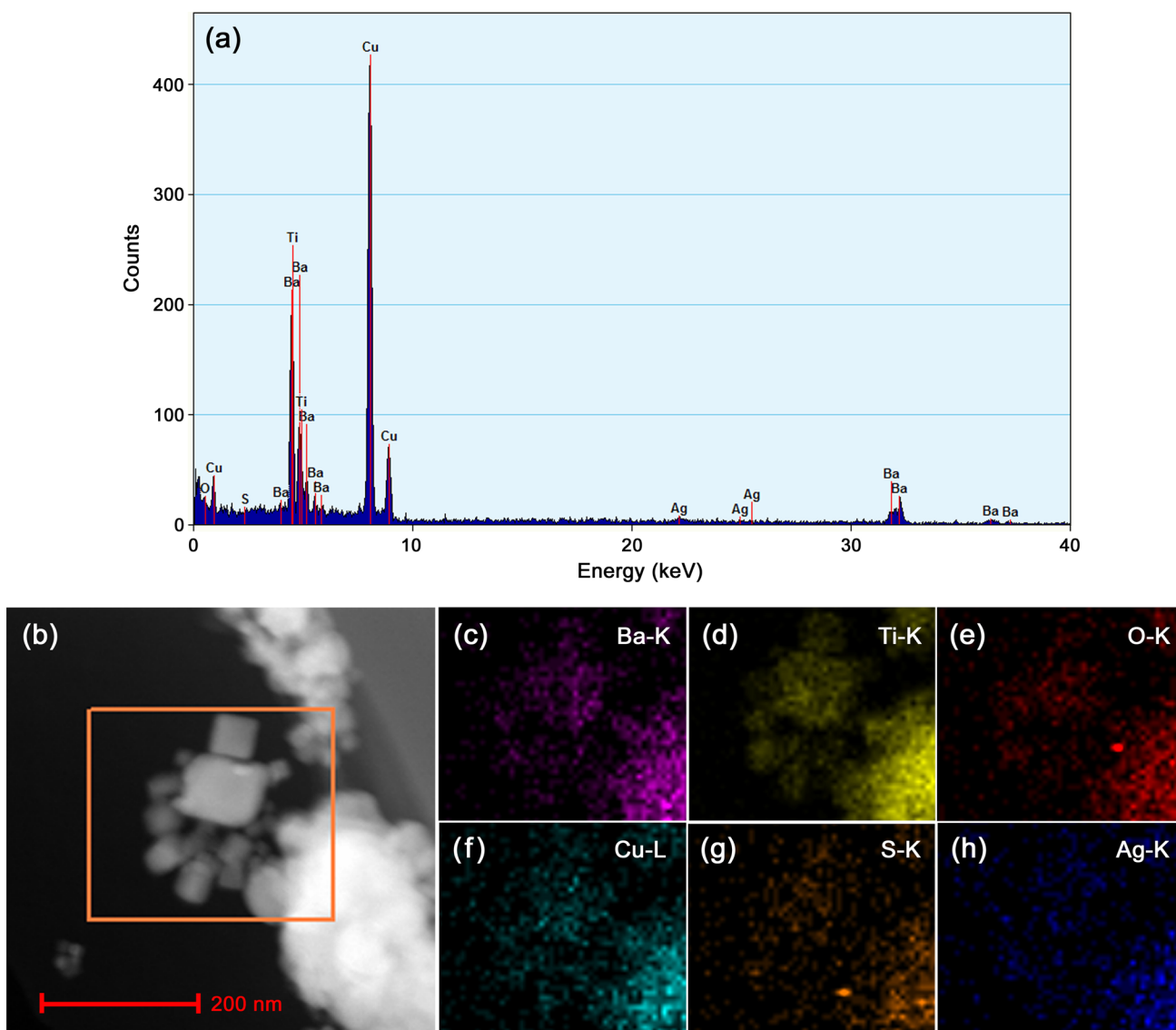


Fig. 5. EDS spectrum (a), DF-STEM image (b) and EDS elemental mapping images (c–h) of 5%CuS/(1%Ag/BTO).

fitted according to the equation  $\ln(C_t/C_0) = -k_{app}t$ , where  $k_{app}$  is known as the apparent first-order reaction rate constant.<sup>33</sup> The derived values of  $k_{app}$  are presented in Table I, which can qualitatively reflect the photodegradation capacities of the samples. It is seen that the photoactivity of the 5%CuS/(1%Ag/BTO) composite is approximately 3.3 and 2.0 times that of bare BaTiO<sub>3</sub> and CuS, respectively. Among the photocatalysts developed in our research group, the 5%CuS/(1%Ag/BTO) composite photocatalyst does not exhibit the highest photodegradation performance, but it still has an advantage in photocatalytically degrading environmental pollutants, such as good photo-corrosive resistance.

The 5%CuS/(1%Ag/BTO) composite was repeatedly employed for the photocatalytic decomposition of RhB in order to examine its reusability. The procedure for the recycling photocatalytic experiment was described in detail in our other

publications.<sup>33</sup> As seen from Fig. 9c, the composite photocatalyst maintains a high photodegradation of RhB after four times of repetitive use ( $\eta = 80.0\%$ ), and only 5.6% of the dye degradation is lost when compared with the first photodegradation cycling ( $\eta = 85.6\%$ ). This slight decrease in the dye degradation can be ascribed to the minor loss of photocatalyst during the recycling process. The recycling experiment suggests the 5%CuS/(1%Ag/BTO) composite photocatalyst exhibits a good photocatalytic reusability, which is superior to many other photocatalysts. For example, the highly active Ag-based semiconductor photocatalysts generally exhibit a poor photocatalytic reusability due to their photo-corrosion.<sup>51</sup>

To reveal the reactive species involved in the 5%CuS/(1%Ag/BTO) photoreactive system, isopropyl alcohol (IPA), methyl alcohol (MeOH) and benzoquinone (BQ) were employed to trap the



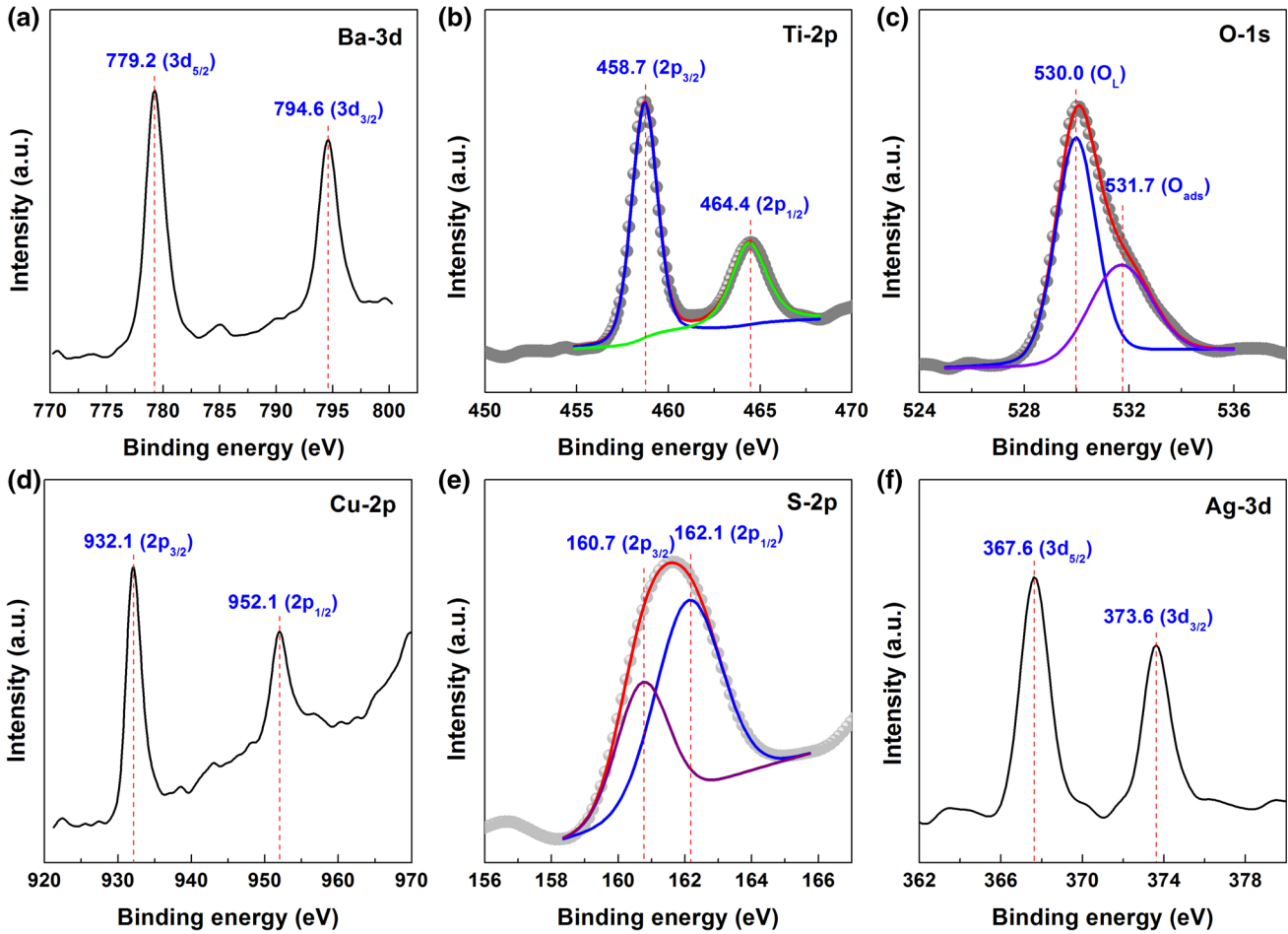


Fig. 6. High-resolution XPS spectra of (a) Ba-3d, (b) Ti-2p, (c) O-1s, (d) Cu-2p, (e) S-2p and (f) Ag-3d core levels for 5%CuS/(1%Ag/BTO).

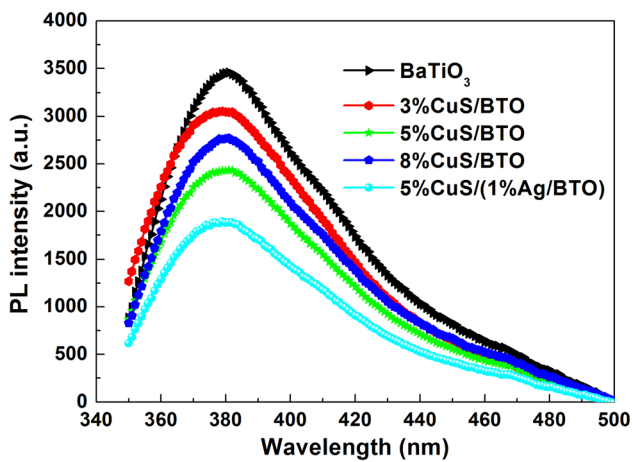


Fig. 7. PL spectra of BaTiO<sub>3</sub>, 3%CuS/BTO, 5%CuS/BTO, 8%CuS/BTO and 5%CuS/(1%Ag/BTO).

hydroxyl (OH<sup>•</sup>), photoexcited  $h^+$  and superoxide (O<sub>2</sub><sup>-</sup>) radicals, respectively. The radical trapping experiments were performed according to the procedure elaborated in our other publications.<sup>52</sup> As displayed in Fig. 9d, the photodegradation percentages of RhB (120 min photocatalysis) are observed to be 38.0%, 57.1% and 69.4% on the introduction of

IPA, MeOH and BQ, respectively. It is obvious that all the scavengers cause an inhibition of the dye degradation, suggesting the dependence of the dye degradation on OH<sup>•</sup>,  $h^+$  and O<sub>2</sub><sup>-</sup> species.

Mott-Schottky method based on the electrochemical measurements in the dark can be available for the estimation of the CB and VB potentials of semiconductors.<sup>6,53</sup> The Mott-Schottky plots derived from BaTiO<sub>3</sub> and CuS (measured frequency 5000 Hz) are displayed in Fig. 10a and b, respectively. By linearly extrapolating the Mott-Schottky plots to the abscissa axis, the flat band potential ( $V_{FB}$ ) of BaTiO<sub>3</sub> and CuS is obtained as -0.92 and +0.86 V versus SCE, respectively. The flat band potential of BaTiO<sub>3</sub> approximately equals its CB edge potential due to its *n*-type semiconductivity (positive slope of the Mott-Schottky plot), whereas the flat band potential of CuS approximately equals its VB edge potential due to its *p*-type semiconductivity (negative slope of the Mott-Schottky plot). With reference to normal hydrogen electrode (NHE), the CB/VB potentials of BaTiO<sub>3</sub> are estimated to be -0.27/+2.99 V, and the CB/VB potentials of CuS are derived to be -0.50/+1.52 V (the relationship between NHE and SCE:  $V_{NHE} = V_{SCE} + 0.059 \times \text{pH}(=7) + 0.242$ ).<sup>6</sup>

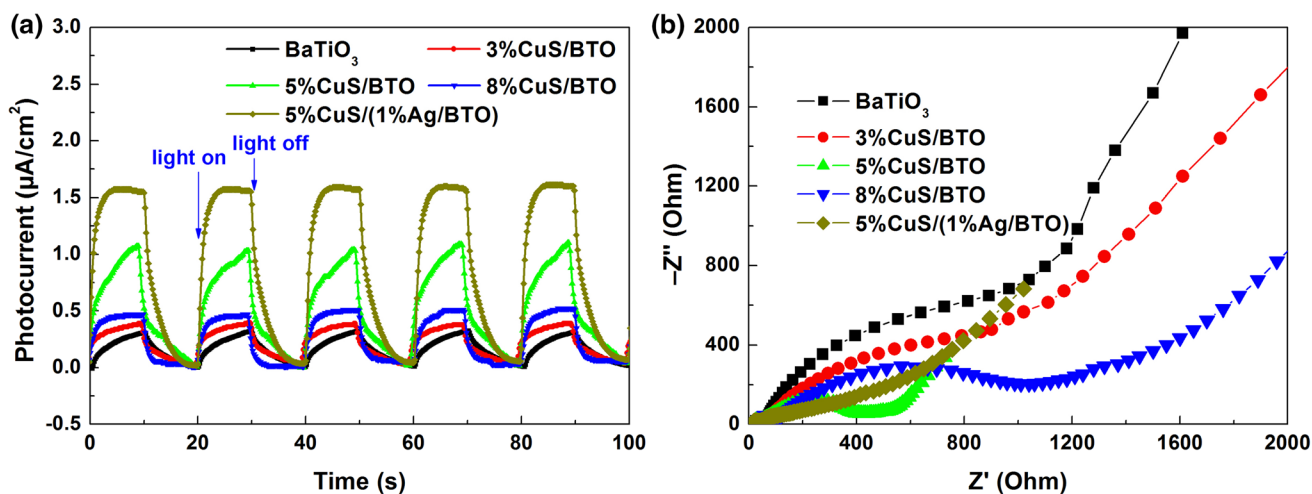


Fig. 8. Transient photocurrent-time curves (a) and EIS Nyquist spectra (b) of the photocatalysts BaTiO<sub>3</sub>, 3%CuS/BTO, 5%CuS/BTO, 8%CuS/BTO and 5%CuS/(1%Ag/BTO).

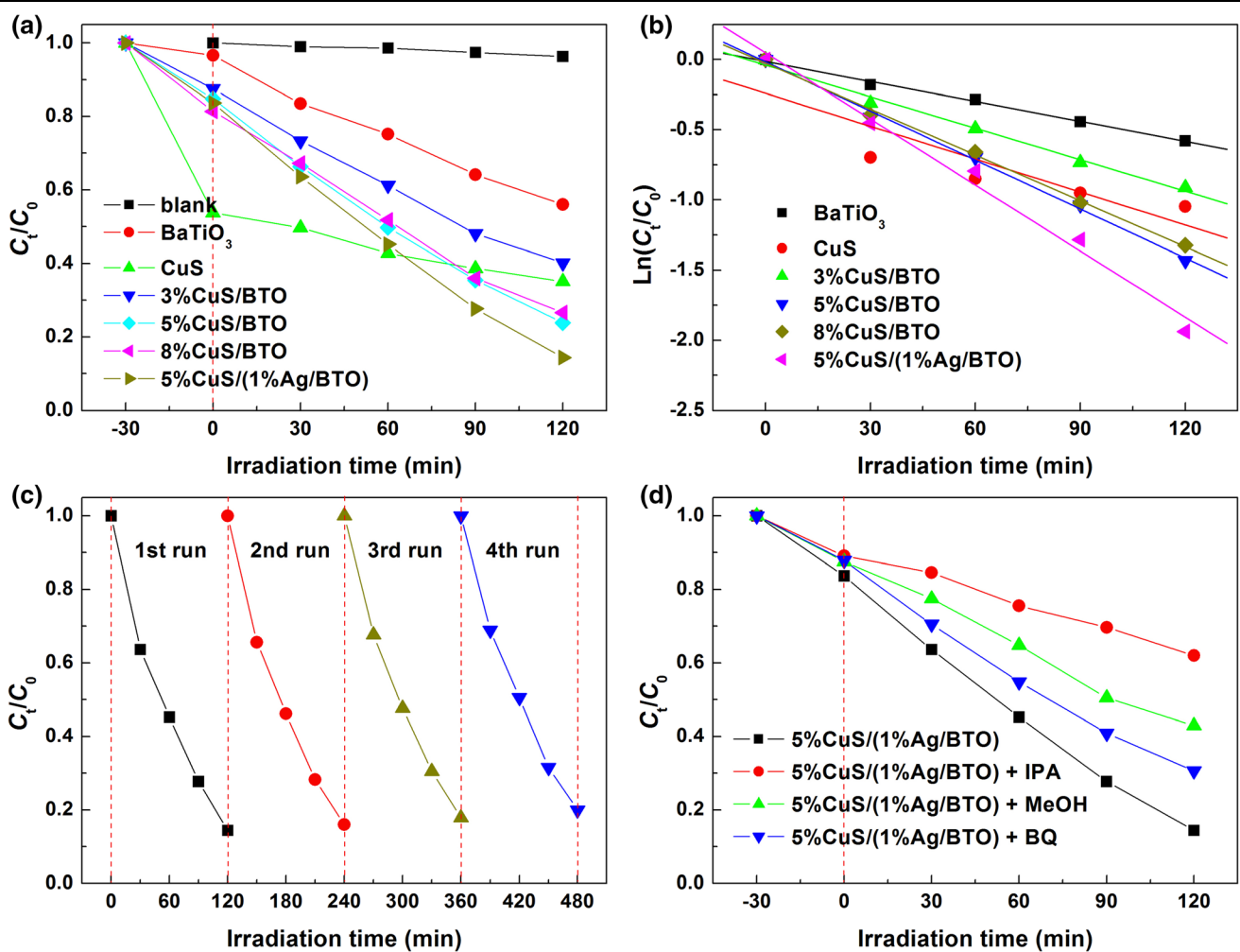


Fig. 9. (a) Adsorption and photodegradation plots of RhB over all the as-prepared samples. (b) Photodegradation kinetic plots for all samples. (c) Reusability of 5%CuS/(1%Ag/BTO) for photocatalytic degradation of RhB. (d) Influence of the scavengers on the photodegradation of RhB over 5%CuS/(1%Ag/BTO).

The possible mechanisms of the binary CuS/BTO and ternary CuS/Ag/BTO composites for enhanced photodegradation of RhB are proposed in Fig. 11. When CuS nanoparticles are decorated onto BaTiO<sub>3</sub> polyhedra, spontaneous electron diffusion from *n*-type BaTiO<sub>3</sub> to *p*-type CuS (hole diffusion from *p*-type CuS to *n*-type BaTiO<sub>3</sub>) occurs at the constructed CuS/BTO heterojunctions. This carrier diffusion process generates an internal electric field at the CuS/BTO interface (positive charge centers at the interface of

BaTiO<sub>3</sub> and negative charge centers at the interface of CuS), which prevents the continuous carrier diffusion. Finally, the CuS/BTO heterojunctions reach a thermal equilibrium state. During the photocatalytic process, both BaTiO<sub>3</sub> and CuS are photoexcited to produce VB holes and CB electrons. Considering that the CB and VB potentials of CuS are respectively negative to those of BaTiO<sub>3</sub>, the photoexcited electrons will be driven by the internal electric field from the CB of CuS to the CB of BaTiO<sub>3</sub>, and conversely, the photoexcited holes from the VB of BaTiO<sub>3</sub> to the VB of CuS, as schematically depicted in Fig. 11a. This transfer process of electrons/holes prolongs their lifetime, consequently making them participate in the photodegradation reactions more efficiently. This is the dominant mechanism resulting in the enhanced photoactivities of the CuS/BTO composites compared to bare BaTiO<sub>3</sub> and CuS. The accumulated electrons in the CB of BaTiO<sub>3</sub> are coupled to O<sub>2</sub> species to form  $\cdot\text{O}_2^-$  radicals, as expected, because of their sufficiently negative potential ( $-0.27\text{ V}$ ) with respect to  $E^0(\text{O}_2/\text{O}_2^-) = -0.13\text{ V}$  versus NHE.<sup>54</sup> It is noted that only some of the VB holes in BaTiO<sub>3</sub> can be transferred to the VB of CuS

**Table I. Photodegradation ratio ( $\eta$ ) of RhB with 180 min reaction and apparent first-order reaction rate constant ( $k_{\text{app}}$ ) for all the as-prepared samples.**

| Samples            | $\eta$ (%) | $k_{\text{app}}$ (min <sup>-1</sup> ) |
|--------------------|------------|---------------------------------------|
| BaTiO <sub>3</sub> | 44.0       | 0.00474                               |
| CuS                | 64.9       | 0.00781                               |
| 3%CuS/BTO          | 59.8       | 0.00749                               |
| 5%CuS/BTO          | 76.1       | 0.01164                               |
| 8%CuS/BTO          | 73.4       | 0.0109                                |
| 5%CuS/(1%Ag/BTO)   | 85.6       | 0.01568                               |

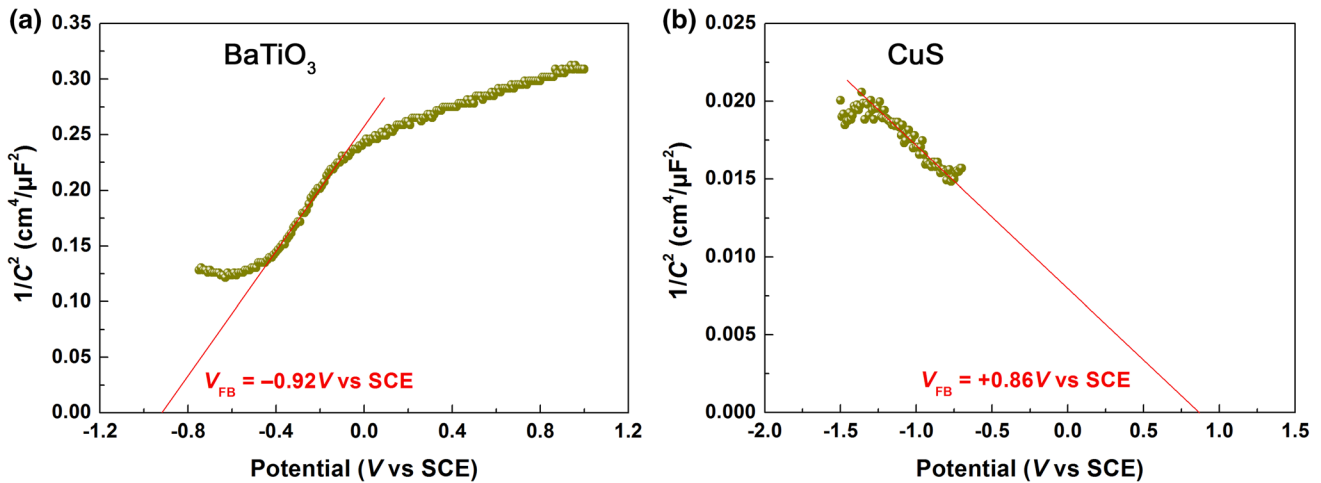


Fig. 10. Mott-Schottky plots of (a) BaTiO<sub>3</sub> and (b) CuS.

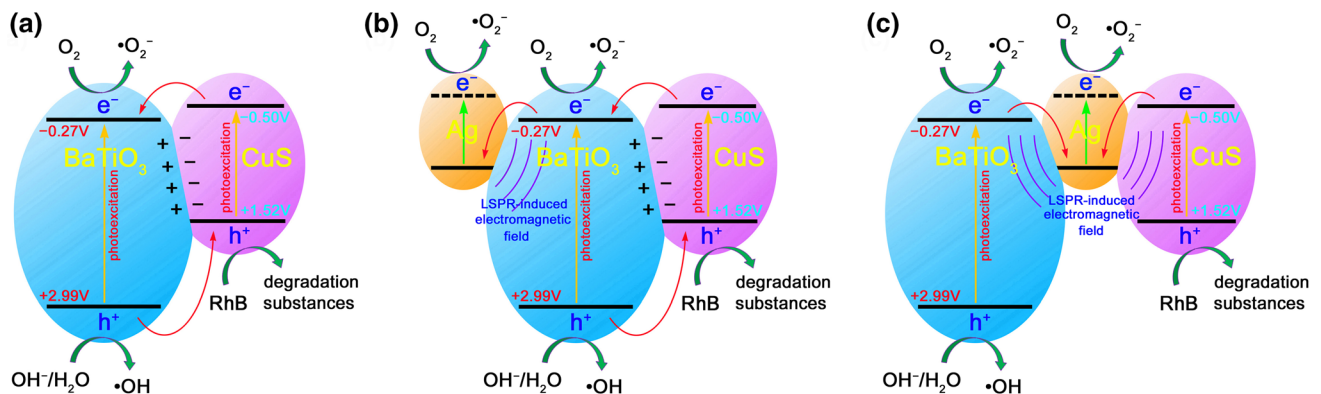


Fig. 11. Possible photodegradation mechanisms of (a) binary CuS/BTO composites and (b, c) ternary CuS/Ag/BTO composites.

because CuS occupies only a small fraction of the CuS/BTO composites. The remaining holes in the BaTiO<sub>3</sub> VB possess a potential (+ 2.99 V) that is more positive than  $E^0(\text{OH}^-/\text{OH}) = +1.99 \text{ V}$  and  $E^0(\text{H}_2\text{O}/\text{OH}) = +2.38 \text{ V}$  versus NHE,<sup>54</sup> suggesting that they are able to react with OH<sup>-</sup> or H<sub>2</sub>O species to produce OH radicals, whereas the accumulated holes in the VB of CuS directly participate in the oxidative degradation reactions with RhB.

The introduction of Ag nanoparticles onto the CuS/BTO composites results in the further increase in their photodegradation performances. There are two locations for the Ag nanoparticles. One is that Ag nanoparticles are located on the surface of BaTiO<sub>3</sub> polyhedra without contacting the CuS nanoparticles, as shown in Fig. 11b. Because of their excellent electron-trapping ability, Ag nanoparticles will capture the CB electrons in BaTiO<sub>3</sub> to make the further reduction of the  $e^-/h^+$  recombination probability in BaTiO<sub>3</sub>. Ag nanoparticles can be also photoexcited under simulated-sunlight irradiation to generate free electrons, which may play a role in the photoreactions. Furthermore, the Ag-LSPR-induced electromagnetic field can stimulate the excitation of BaTiO<sub>3</sub> to produce additional electrons and holes. Another location for Ag nanoparticles sandwiched between BaTiO<sub>3</sub> and CuS, as depicted in Fig. 11c. In this case, the CB electrons in both BaTiO<sub>3</sub> and CuS are trapped by Ag nanoparticles, thus promoting the  $e^-/h^+$  separation. Meanwhile, both BaTiO<sub>3</sub> and CuS can benefit from the LSPR of Ag nanoparticles to produce more  $e^-/h^+$  pairs.

## CONCLUSIONS

In this work, CuS/BTO and CuS/Ag/BTO composite photocatalysts have been developed. In these composites, CuS and Ag nanoparticles are anchored on the surface of BaTiO<sub>3</sub> polyhedra. Compared with bare BaTiO<sub>3</sub> and CuS, the as-developed composite photocatalysts obviously exhibit enhanced simulated-sunlight photodegradation towards RhB. The highest photoactivity is observed for the 5%CuS/(1%Ag/BTO) composite, which is increased to about 3.3 and 2.0 times as compared with that of bare BaTiO<sub>3</sub> and CuS, respectively. Efficient  $e^-/h^+$  separation resulting from carrier transfer process and LSPR effect of Ag nanoparticles are available for interpreting the enhanced photodegradation of RhB by the CuS/Ag/BTO composites.

## FUNDING

This study was funded by the National Natural Science Foundation of China (Grant No. 51662027) and the Scientific Research Fund of Sichuan Provincial Science and Technology Department (Grant No. 2020YJ0137).

## CONFLICT OF INTEREST

The authors declare that they have no conflict of interest.

## REFERENCES

1. Z.M. He, Y.M. Xia, J.B. Su, and B. Tang, *Opt. Mater.*, 88, 195 (2019).
2. S.F. Wang, Y. Wang, H.J. Gao, J.Y. Li, L.M. Fang, X.L. Yu, S.N. Tang, and X.X. Zhao, *Optik*, 221, 165363 (2020).
3. Y.X. Yan, H. Yang, X.X. Zhao, H.M. Zhang, and J.L. Jiang, *J. Electron. Mater.*, 47, 3045 (2018).
4. C. Berberidou, V. Kitsiou, D.A. Lambropoulou, A. Antoniadis, E. Ntonou, G.C. Zalidis, and I. Poullos, *J. Environ. Manag.*, 195, 133 (2017).
5. J.Y. Li, S.F. Wang, G. Sun, H.J. Gao, X.L. Yu, S.N. Tang, X.X. Zhao, Z. Yi, Y. Wang, and Y. Wei, *Mater. Today Chem.*, 19, 100390 (2021).
6. S.Y. Wang, H. Yang, Z. Yi, and X.X. Wang, *J. Environ. Manag.*, 248, 109341 (2019).
7. M. Ahmadi, H.R. Motlagh, N. Jaafarzadeh, A. Mostoufi, R. Saeedi, G. Barzegar, and S. Jorfi, *J. Environ. Manag.*, 186, 55 (2017).
8. Q.Q. Duan, J.Y. Jia, X. Hong, Y.C. Fu, C.Y. Wang, K. Zhou, X.Q. Liu, H. Yang, and Z.Y. Wang, *Sol. Energy*, 201, 555 (2020).
9. Y.M. Xia, Z.M. He, J.B. Su, and K.J. Hu, *J. Mater. Sci.-Mater. Electron.*, 30, 9843 (2019).
10. S.T. Guan, H. Yang, X.F. Sun, and T. Xian, *Opt. Mater.*, 100, 109644 (2020).
11. K. Kaur, R. Badru, P.P. Singh, and S. Kaushal, *J. Environ. Chem. Eng.*, 8, 103666 (2020).
12. T. Xian, X.F. Sun, L.J. Di, H.Q. Li, and H. Yang, *Opt. Mater.*, 111, 110614 (2021).
13. H.J. Gao, X.X. Zhao, H.M. Zhang, J.F. Chen, S.F. Wang, and H. Yang, *J. Electron. Mater.*, 49, 5248 (2020).
14. M. Karmaoui, L. Lajaunie, D.M. Tobaldi, G. Leonardi, C. Benbayer, R. Arenal, and J.A. Labrincha, *Appl. Catal. B-Environ.*, 218, 370 (2017).
15. H.J. Gao, F. Wang, S.F. Wang, X.X. Wang, Z. Yi, and H. Yang, *Mater. Res. Bull.*, 115, 140 (2019).
16. M. Rastogi, C. Bowen, H.S. Kushwaha, and R. Vaish, *Mater. Sci. Semicond. Proc.*, 51, 33 (2016).
17. P.Q. Yu, H. Yang, X.F. Chen, Z. Yi, W.T. Yao, J.F. Chen, Y.G. Yi, and P.H. Wu, *Renew. Energy*, 158, 227 (2020).
18. L.Y. Jiang, C. Yuan, Z.Y. Li, J. Su, Z. Yi, W.T. Yao, P.P. Wu, Z.M. Liu, S.B. Cheng, and M. Pan, *Diam. Relat. Mater.*, 111, 108227 (2021).
19. S.U. Lu, L. Xia, J.M. Xu, C.H. Ding, T.T. Li, H. Yang, B. Zhong, T. Zhang, L.N. Huang, L. Xiong, X.X. Huang, and G.W. Wen, *ACS Appl. Mater. Interfaces*, 11, 18626 (2019).
20. G.S. Ma, Y.B. Chen, L. Xia, Y.F. Zhan, B. Zhong, H. Yang, L.N. Huang, L. Xiong, X.X. Huang, and G.W. Wen, *Ceram. Int.*, 46, 10903 (2020).
21. X.X. Wang, J.K. Zhu, H. Tong, X.D. Yang, X.X. Wu, Z.Y. Pang, H. Yang, and Y.P. Qi, *Chin. Phys. B*, 28, 044201 (2019).
22. X.X. Wang, Y. Wu, X.L. Wen, J.K. Zhu, X.L. Bai, Y.P. Qi, and H. Yang, *Opt. Quantum Electron.*, 52, 238 (2020).
23. K. Saeed, N. Zada, and I. Khan, *Sep. Sci. Technol.*, 54, 2729 (2019).
24. S.F. Wang, H.J. Gao, X.L. Yu, S.N. Tang, Y. Wang, L.M. Fang, X.X. Zhao, J.Y. Li, L. Yang, and W.Q. Dang, *J. Mater. Sci. Mater. Electron.*, 31, 17736 (2020).
25. X.X. Zhao, H. Yang, S.H. Li, Z.M. Cui, and C.R. Zhang, *Mater. Res. Bull.*, 107, 180 (2018).
26. F. Cordero, F. Cordero, *J. Appl. Phys.*, 123, 094103 (2018).
27. A.A. Yadav, Y.M. Hunge, V.L. Mathe, and S.B. Kulkarni, *J. Mater. Sci.-Mater. Electron.*, 29, 15069 (2018).
28. S. Kumar, M. Sharma, S. Powar, E.N. Kabachkov, and R. Vaish, *J. Eur. Ceram. Soc.*, 39, 2915 (2019).

29. Y.B. Zhang, Z. Yi, X.Y. Wang, P.X. Chu, W.T. Yao, Z.G. Zhou, S.B. Cheng, Z.M. Liu, P.H. Wu, M. Pan, and Y.G. Yi, *Phys. E*, 127, 114526 (2021).
30. Z. Yi, J.K. Li, J.C. Lin, F. Qin, X.F. Chen, W.T. Yao, Z.M. Liu, S.B. Cheng, P.H. Wu, and H.L. Li, *Nanoscale*, 12, 23077 (2020).
31. Z. Hosseinpour, A. Alemi, A.A. Khandar, X. Zhao, and Y. Xie, *New J. Chem.*, 39, 5470 (2015).
32. J. Kundu and D. Pradhan, *ACS Appl. Mater. Interfaces*, 6, 1823 (2014).
33. Y.P. Wang, H. Yang, X.F. Sun, H.M. Zhang, and T. Xian, *Mater. Res. Bull.*, 124, 110754 (2020).
34. T.A. Kurniawan, Y.Y. Lin, O. Tong, A.B. Albadarin, and G. Walker, *Mater. Sci. Semicond. Proc.*, 73, 42 (2018).
35. P.M. Nithya, and L.G. Devi, *Surf. Interfaces*, 15, 205 (2019).
36. M. Basu, N. Garg, and A.K. Ganguli, *J. Mater. Chem. A*, 2, 7517 (2014).
37. M. Basu, R. Nazir, P. Fageria, and S. Pande, *Sci. Rep.*, 6, 34738 (2016).
38. S.T. Guan, R.S. Li, X.F. Sun, T. Xian, and H. Yang, *Mater. Technol.* <https://doi.org/10.1080/10667857.2020.1782062> (2020).
39. P.X. Chu, J.X. Chen, Z.G. Xiong, and Z. Yi, *Opt. Commun.*, 476, 126338 (2020).
40. X.X. Wang, J.K. Zhu, Y.Q. Xu, Y.P. Qi, L.P. Zhang, H. Yang, and Z. Yi, *Chinese Phys. B*, 30, 024207 (2021).
41. X.F. Sun, L.J. Di, T. Xian, Y.J. Zhou, H.Q. Li, Y.S. Gao, and H. Yang, *J. Mater. Sci.-Mater. Electron.* <https://doi.org/10.1007/s10854-020-04844-z> (2020).
42. J. Tauc, R. Grigorovici, and A. Vancu, *Phys. Status Solidi* 15, 627 (1966).
43. S.F. Wang, H.J. Gao, G.Z. Sun, Y. Wang, L.M. Fang, L. Yang, L. Lei, and Y. Wei, *Russ. J. Phys. Chem. A*, 94, 1234 (2020).
44. M.R. Khalifeh, H. Shokrollahi, S.M. Arab, and H. Yang, *Mater. Chem. Phys.*, 247, 122838 (2020).
45. L. Gomathi Devi, and P.M. Nithya, *J. Environ. Chem. Eng.*, 6, 3565 (2018).
46. M. Golkari, H. Shokrollahi, and H. Yang, *Ceram. Int.*, 46, 8553 (2020).
47. Y.P. Wang, X.F. Sun, T. Xian, G.R. Liu, and H. Yang, *Opt. Mater.*, 113, 110853 (2021).
48. S.N. Tang, S.F. Wang, X.L. Yu, H.J. Gao, X.W. Niu, Y. Wang, X.X. Zhao, G.Z. Sun, and D.F. Li, *Chem. Select*, 5, 10599 (2020).
49. M.D. Stoller, S.J. Park, Y.W. Zhu, J.H. An, and R.S. Ruoff, *Nano Lett.*, 8, 3498 (2008).
50. G. Corro, F. Banuelos, E. Vidal, and S. Cebada, *Fuel*, 115, 625 (2014).
51. Y. Bi, S. Ouyang, N. Umezawa, J. Cao, and J. Ye, *J. Am. Chem. Soc.*, 133, 6490 (2011).
52. Y.M. Xia, Z.M. He, J.B. Su, S.Q. Zhu, and B. Tang, *J. Electron. Mater.*, 49, 3259 (2020).
53. S.J. Hong, S. Lee, J.S. Jang, and J.S. Lee, *Energy Environ. Sci.*, 4, 1781 (2011).
54. T.T. Cheng, X.F. Sun, T. Xian, Z. Yi, R.S. Li, X.X. Wang, and H. Yang, *Opt. Mater.*, 112, 110781 (2021).

**Publisher's Note** Springer Nature remains neutral with regard to jurisdictional claims in published maps and institutional affiliations.